Accepted Manuscript

Title: Detailed investigation of defect states in Erbium doped In_2O_3 thin films

Authors: Anupam Ghosh, Shyam Murli Manohar Dhar Dwivedi, Shubhro Chakrabartty, Mohamed Henini, Aniruddha Mondal

PII: S0025-5408(17)32056-1
DOI: https://doi.org/10.1016/j.materresbull.2017.11.020
Reference: MRB 9678

To appear in: *MRB*

Received date: 25-5-2017
Revised date: 1-11-2017
Accepted date: 9-11-2017

Please cite this article as: Anupam Ghosh, Shyam Murli Manohar Dhar Dwivedi, Shubhro Chakrabartty, Mohamed Henini, Aniruddha Mondal, Detailed investigation of defect states in Erbium doped In2O3 thin films, Materials Research Bulletin https://doi.org/10.1016/j.materresbull.2017.11.020

Detailed investigation of defect states in Erbium doped In_2O_3 thin films

Anupam Ghosh[1], Shyam Murli Manohar Dhar Dwivedi[1], Shubhro Chakrabartty[1], Mohamed Henini[2] and Aniruddha Mondal[1,*]

[1]Department of Physics, National Institute of Technology Durgapur, Durgapur - 713209, India.

[2]School of Physics and Astronomy, Nottingham Nanotechnology and Nanoscience Center, University of Nottingham, Nottingham NG7 2RD, United Kingdom

[*]Corresponding author e-mail: aniruddhamo@gmail.com

Graphical Abstract:

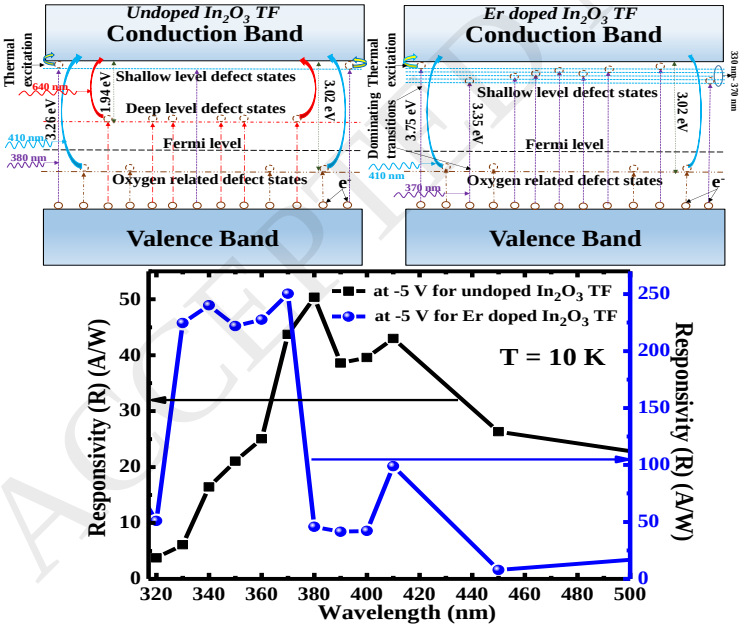

Highlights

- SIMS analysis confirmed the doping of Er into the In_2O_3 TF
- I-V loop analysis gives reduced current memory window for In_2O_3:Er TF based device
- High ideality factor was determined at low temperature and explained
- Defect related photoconductivity was confirmed from low temperature measurement
- 10 K temporal response of the Au/In_2O_3:Er/Si confirmed removal of oxygen defects

Abstract:

Erbium doped Indium Oxide (In_2O_3:Er) thin films (TFs) were synthesised by spin-on technique. Secondary Ion Mass Spectrometry confirmed that Er is incorporated into the In_2O_3 lattice and formed an In-O-Er layer. The current –voltage loop produced a lower loop current window of ~3.6 x10^{-4} A for In_2O_3:Er TF based devices. The Au/In_2O_3:Er/Si Schottky devices have lower ideality factor (~6) and higher barrier height (~0.63 eV) at 300 K than Au/In_2O_3/Si control samples. A blue shift in the main band-gap (~50 nm) was calculated for In_2O_3:Er TFs from 10 K photoresponse. The Au/In_2O_3:Er/Si samples show higher photosensitivity in the temperature range 10 K -300 K and maximum (~15 times) in the UV region at 10 K as compared to the Au/In_2O_3/Si devices. In addition, the Au/In_2O_3:Er/Si devices have better UV to visible cut-off ratio (~3 times). Excellent temporal responses were recorded for Au/In_2O_3:Er/Si in the UV region as compared to Au/In_2O_3/Si.

Keywords: A. electronic materials; A. oxides; B. chemical synthesis; D. defects; D. electrical properties.

1. Introduction:

Metal oxide semiconductor (MOS) thin films (TFs) are important for the fabrication of transparent optoelectronic devices [1]. Amongst MOS based materials, Indium Oxide (In_2O_3) is a better transparent oxide semiconductor (TOS) material compared to other well-known materials such as TiO_2 and ZnO because of its high carrier mobility (~43.7 cm^2/V-s) [2] and wide direct bandgap of 3.5 – 3.7 eV [3]. The detection of ultraviolet (UV) light is also very important for applications in flame sensors, missile plume detectors, spatial optical communication devices, UV photosensors, biological and chemical sensors, laser-based devices etc. [4]. In spite of the encouraging results reported, the carrier concentration in MOS devices is difficult to control due to the presence of large numbers of oxygen vacancies and defects [5,6] which results in non-reliable performance of optoelectronic devices. A major breakthrough in this field was the epitaxial growth of single crystal TOS (Indium Gallium Zinc Oxide) TFs with an atomically flat surface on yttria-stabilized zirconia substrates [7]. However, the reduction in oxygen vacancies in TOS as well as compatibility with existing Silicon technology by cost-effective techniques is challenging [4]. Inorganic materials activated with rare earth ions (REs) have suitable spectroscopic characteristics to design luminescent or display materials [8]. Use of REs with TOSs is receiving much interest in scientific community due to the wide range of technological applications based on their increased transparency in the visible region (Sc or Y doped ZnO) [9], intra-ionic radiative transition processes (Er doped In_2O_3) [10], increased photosensitivity or photo-emissivity (Er doped SnO_2 and Erbium Tin Oxide) [11], bandgap engineering (Ga^{3+} doped $Lu_3Al_5O_{12}$) [12], enhanced photocatalytic activity (Er^{3+} doped β-Bi_2O_3) [13], defect engineering (Praseodymium doped GaN) [14], reduction of the oxygen and N related defects by Er [15] etc. Amongst these REs, Erbium (Er) is optically active f- block element and can emit photon

corresponding to the wavelength of ~1540 nm, which lies in the region of minimum losses for silica-based waveguides used in fibre optic communications [16–19] and silicon photonics [20]. Researchers also reported on the improved detection of UV light by Er doped In_2O_3 (In_2O_3:Er) TFs as compared to undoped In_2O_3 TFs and investigated the removal of oxygen-related defect states from the host In_2O_3 material using optical and electrical techniques [4]. However, it is important to find out the energy positions of the defect states within the bandgap of In_2O_3 after incorporation of Er atoms and their roles in device performance. Amongst all the defects identified in TOSs, oxygen vacancy is one of the most significant and is considered to be the dominant defect in In_2O_3. Oxygen vacancies in MOS had been investigated extensively both experimentally [21–23] and theoretically [24,25]. For example, low-temperature photo-capacitance and photocurrent measurements were performed to study defects introduced in GaAs by N incorporation [15]. However, there are no reports on the investigation of defects using temperature dependent current– voltage (I-V) characteristics, photosensitivity and low temperature temporal responses of In_2O_3:Er TFs, which is important for improving their performance as UV detectors.

In this paper, the doping of Er into In_2O_3 lattice has been confirmed by Secondary Ion Mass Spectrometry (SIMS) analysis. We have performed I-V hysteresis, temperature dependent (10 K- 300 K) photosensitivity, low temperature (10 K) responsivity and low temperature (10 K) temporal response of detectors in order to probe the energy positions of the defects present in undoped In_2O_3 and In_2O_3:Er TFs. The theoretical analysis of the ideality factor (η) and barrier height (Φ_B) was performed using Schottky model by taking into consideration the presence of defects. Low-temperature photocurrent and temporal responses provided the information about the type of defects and energy level positions.

2. Experimental Details:

2.1 Synthesis of Undoped and Er doped In_2O_3 TFs and device fabrication:

In_2O_3 and In_2O_3:Er TFs were deposited on RCA cleaned p-type Si (100) substrates (resistivity ~10 Ω-cm, MTI, USA) by spin coating technique using the chemical route [4]. The sol-gel for In_2O_3 TF was prepared by dissolving 0.5 g Indium (III) Chloride ($InCl_3$) anhydrous powder (5 N purity, Sigma-Aldrich) into 30 ml of acetylacetone (purity> 99%, Merck) under ultrasonication (~50 ^{0}C, 15 min) and left for ageing for 24 h. It was then spin coated (spin NXG-P1, apexicindia) on the Si substrate (rotation speed ~1000 rpm for 1 min). The as-deposited film was then annealed in a muffle furnace (~400 ^{0}C for 10 min) under atmospheric air condition. The entire process was repeated four times in order to get a uniform film over the substrate with final annealing at ~400 ^{0}C for 30 min. To prepare In_2O_3:Er solution, 0.04 g Erbium (III) Oxide nanopowder (purity≥ 99.9%, Aldrich) was dissolved in 10 ml sulfuric acid (H_2SO_4) by ultrasonication (~50 ^{0}C, 15 min) and finally added to the previously prepared $InCl_3$ solution. This doped solution was ultrasonicated (~50 ^{0}C, 15 min) and left for 48 h for ageing. The In_2O_3:Er sol-gel was then spin-coated on a p-Si substrate (rotation speed ~6000 rpm for 2 min) followed by 10 min open air annealing (~400 ^{0}C) for four times with final annealing at ~400 ^{0}C for 30 min as has already been described. Gold (Au) was evaporated through circular holes of an aluminum mask, which was placed on top of the samples to form the upper electrode (diameter ~2 mm) contact of the Schottky devices by thermal evaporation method. Indium was used as an Ohmic contact on the backside of p-Si substrate. Both the undoped In_2O_3 (Au/In_2O_3/Si) and Er doped In_2O_3 devices (Au/In_2O_3:Er/Si) were prepared using the same procedure.

2.2 Characterisation techniques:

Time-of-Flight Secondary Ion Mass Spectrometry (ToF-SIMS) (PHI TRIFT V nano TOF, Physical Electronics, USA) was performed using dual beam configuration on the undoped and In_2O_3:Er TFs to analyse the depth profiles (using a stylus-based profilometer). A caesium (Cs^{2+}) primary ion beam of 0.3 μA beam current and 3.0 keV net impact energy was used as a

sputtering ion source to etch the sample surface within a raster size of 600 μm x 600 μm, whereas a Gallium (Ga) gun was used to analyse the secondary ions. The SIMS aperture settings were used to restrict secondary ion analysis within the square area within the raster region of 40 μm x 40 μm using liquid metal (Ga) ion gun. This SIMS configuration is used to determine appropriate composition of the TFs [26]. The I–V characteristics of Au/In_2O_3/Si and Au/In_2O_3:Er/Si were investigated using a Keithley 2401 source meter and 300 W Ozone free xenon arc lamp (650-0047). The photocurrent spectra of both detectors were recorded at low temperature using an open beam configuration through a monochromator (120-9055, Science tech Inc., Canada) and a He cryostat (Advanced Research System).

3. Results and discussion:

3.1 SIMS analysis and depth profiling interpretation:

Fig. 1 shows the semi-logarithmic plot of the number of counts of different ions against sputter time and counts vs depth profiles, where the time scale is converted into depth (nanometers) by using a stylus-based profilometer. The inset of Figs. 1(a) and 1(b) shows the CCD images of the TF surface. The undoped In_2O_3 TF displays high surface roughness (inset of Fig. 1(a)), which contains small grains all over the TF surface. The In_2O_3:Er TF (inset of Fig. 1(b)) surface becomes smoother, which was also characterised previously using scanning electron microscopy (SEM) [4].

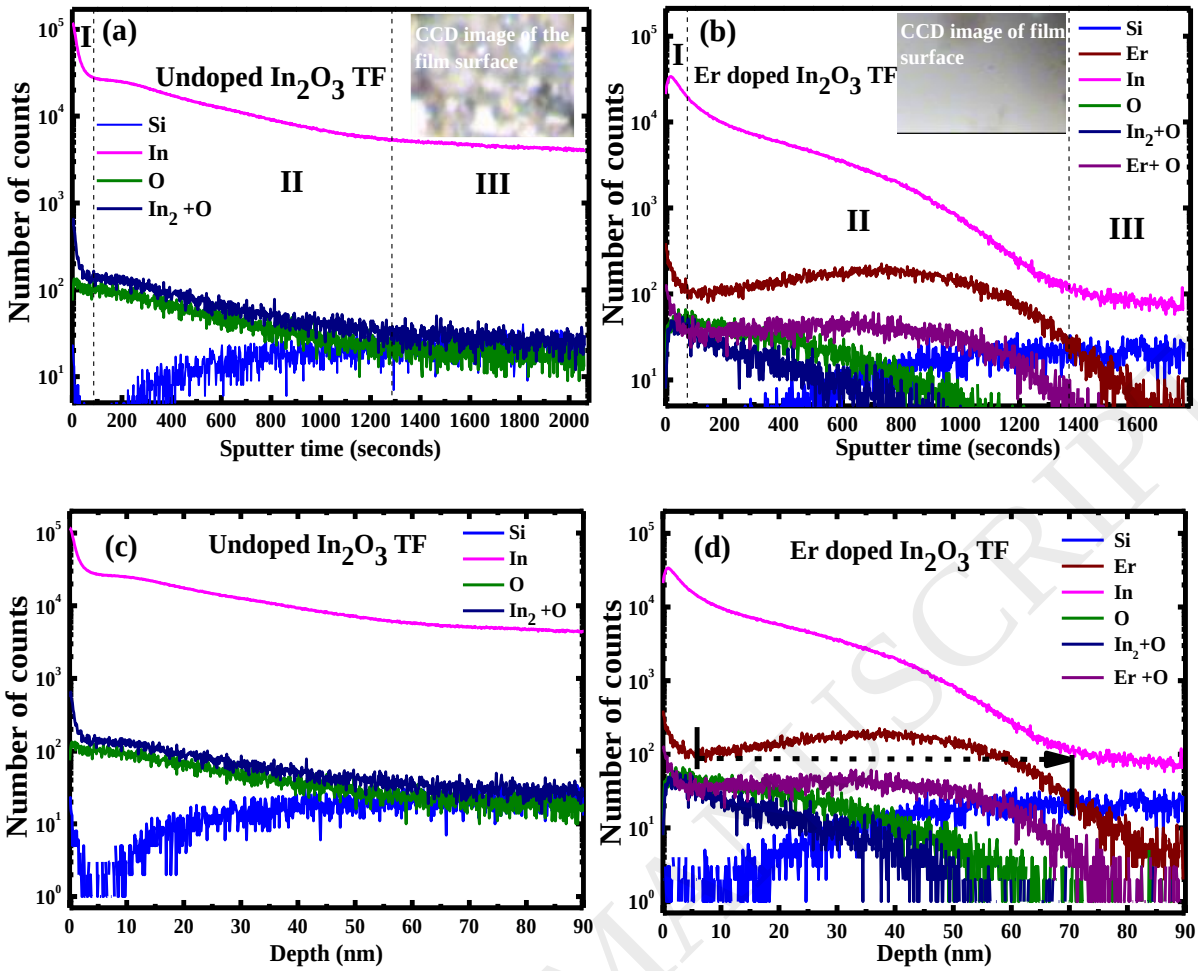

Fig. 1: Sputter time vs. number of counts for (a) undoped In_2O_3 TF (CCD image in inset) and (b) In_2O_3:Er TF (CCD image in inset); depth (in nm) of the TF vs. number of counts for (c) undoped In_2O_3 TF and (d) In_2O_3:Er TF.

The sputter time vs the number of counts spectrum can be divided into three different regions [27]. The region-I is marked for non-equilibrium sputtering of the Cs^{2+} ions on the undoped and In_2O_3:Er TF surfaces, where the number of counts of In, O and In, O, Er etc. decreases rapidly for undoped (Fig. 1(a)) and In_2O_3:Er TFs (Fig. 1(b)), respectively. With the increasing sputter time, in the region-II equilibrium sputtering was achieved. In this region, the incoming sputter ions became equal to the outgoing sputter ions [27]. Therefore, there is a slow decrease in the counts of In (from 27603 to 1286), In_2+O and O for undoped In_2O_3 TF which confirms the formation of stable In_2O_3 TF layer (Fig. 1(a)). In the case of In_2O_3:Er TF, in region-II, In (from 19123 to 1368) and In_2+O ion yield decreases sharply from maximum

value while approaching towards the In_2O_3:Er TF-Si substrate interface (Fig. 1(b)). However, the counts of Er and Er+O are almost parallel to the sputtering time axis in region-II. This observation indicates that Er incorporated into In_2O_3 TF lattice replaces some In and O atoms and form an inhomogeneous In-O-Er layer on the substrate. The background level is indicated by region-III, where diffusion of the dopant species (Er) does not occur and counts of the In element is recorded. The depth profile of undoped TF counts for the elements shows almost parallel variation with depth axis from 5-70 nm, which proves the formation of homogeneous In_2O_3 TF layer over the region (Fig. 1(c)). In the case of In_2O_3:Er TF (Fig. 1(d)), the counts for Er and Er+O are stable, whereas the In and In_2+O contents decrease rapidly from 5 nm to 70 nm depth. Therefore, the diffusion of Er into In_2O_3 lattice basically forms a non-stoichiometric layer of thickness around 65 nm. Beyond the 70 nm depth, the background concentration of In atoms was recorded. The spectra for Si ions appeared due to the Si substrate. The depth profile identifies the diffusion of Er and In atoms into the Si substrate, which may be due to the chemical reaction between the precursors and the Si substrate during the open air annealing process at 400 ^{0}C.

3.2 Presence of memory:

The ten (10) successive loops of I - V characteristics were taken for both Au/In_2O_3/Si and Au/In_2O_3:Er/Si devices to investigate the state of defects present in the material. Fig. 2 demonstrates the 1st and 10th loop of such I-V curves for both devices for DC voltage sweep between +2 V and +5 V. The path 1 and path 2 indicate the currents for the up-sweep and down-sweep between +2 V and +5 V. Fig. 2 (inset) shows the number of I-V loops vs current window curve. The current window for the Au/In_2O_3/Si device reduces from a maximum of 8.6 x10^{-3} A (1st loop) to 1 x 10^{-4} A (10th loop) and for Au/In_2O_3:Er/Si device it reduces from 3.6 x10^{-4} A (1st loop) to 1.7 x10^{-5} A (10th loop) at an applied bias of +3 V. Therefore, the 1st and 10th current loops indicates that the current window reduction ratios are ΔI ~86 and ΔI

~21 for Au/In_2O_3/Si and Au/In_2O_3:Er/Si devices, respectively. Larger current loop memory of the Au/In_2O_3/Si device is observed due to the presence of huge oxygen related

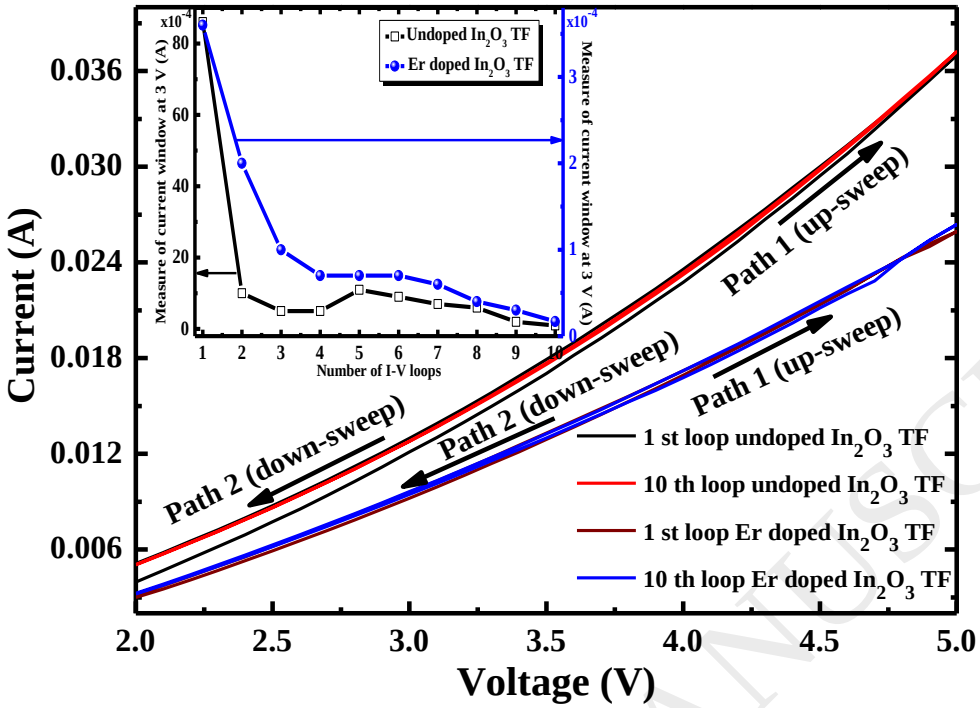

Fig. 2: 1st and 10th loop of I-V curves for both Au/In_2O_3/Si and Au/In_2O_3:Er/Si devices for applied dc voltage of operations between +2 V and +5 V; the number of I-V loops vs. current window curve (inset).

defects [28,29] into the lattice and at the Au/In_2O_3 Schottky interface. Under the forward bias condition, the undoped In_2O_3 TF produces ionisation due to the availability of huge free carriers (~8 x 10^{16} cm^{-3}) [4], which enhances the depletion width at the junction and finally charge storage of the device. On the other hand, incorporation of Er into the In_2O_3 matrix reduces the oxygen-related defect states and traps at the metal-semiconductor interface. The carrier compensation process reduces the free carrier concentration (~5 x 10^{12} cm^{-3}) of the In_2O_3:Er material [4]. Therefore, under the forward bias, the carriers are unable to produce high ionisation and subsequently the depletion width reduces as compared to Au/In_2O_3/Si device. Hence, the charge storage capability of the Au/In_2O_3:Er/Si device, which possesses small current window, is reduced. The number of ionisation carriers is reduced successively after each loop for both devices and therefore the reduction in current memory window is

obtained. A large current loop reduction ratio of ΔI ~86 is obtained for Au/In_2O_3/Si as compared to Au/In_2O_3:Er/Si device (ΔI ~21) due to the availability of huge free carriers for ionization in the 1st loop, which was largely reduced in the 10th loop for the Au/In_2O_3/Si device. These observations suggest that Er doping of In_2O_3 decreases the oxygen-related defect states.

3.3 Temperature dependent characteristics:

The temperature dependent dark ln I -V characteristics of the Au/In_2O_3/Si and Au/In_2O_3:Er/Si devices are shown in Fig. 3(a). It is observed that the reverse saturation current (I_s) exhibits small increase with temperature (T) from 4.2 x 10^{-6} A (at 10 K) to 9.7 x 10^{-6} A (at 300 K) for the Au/In_2O_3/Si device. On the other hand, the I_s increases rapidly with increasing temperature for the Au/In_2O_3:Er/Si device from 1.2 x 10^{-9} A (at 10 K) to 2.1 x 10^{-6} A (at 300 K). The 300 K ideality factor (η) of the Au/In_2O_3/Si device is calculated to be higher (η ~12) than that of Au/In_2O_3:Er/Si device (η ~6) as obtained from the forward I-V characteristics shown in Fig. 3(b) using the equation $\eta = \frac{q}{kT}\left[\frac{\partial V}{\partial(ln\ I)}\right]$ (where, q is the electronic charge, k is the Boltzmann constant, T is the temperature and $\frac{\partial(ln\ I)}{\partial V}$ is the slope of the linear fit of the ln I vs V curve between 0.5 V and 1 V). The presence of large numbers of oxygen-related defect states at the interface of metal-semiconductor increases the carrier tunneling by hole trapping process into the device [30], which in turn enhances the ideality factor. At low temperature (10 K) the maximum η value of ~685 and ~574 are calculated for the Au/In_2O_3/Si and Au/In_2O_3:Er/Si devices, respectively. With the increase in temperature from 10 K to 300 K, there is an exponential decay of η as shown in Fig. 3(b). The η vs. T curves for both undoped (η_1) and doped (η_2) devices are best fitted with the equations: $\eta_1 = y_0 + Ae^{(-T/t_1)} + Be^{(-T/t_2)}$ and $\eta_2 = y_0' + Ce^{(-T/t_3)}$ respectively, where y_0 =15.4, A= 1397.7, B =238.8, t_1= 9.26, t_2 = 47.7 and y_0' = 16.7, C =1929.4, t_3= 8.1. The η values of Au/In_2O_3/Si and

Au/In_2O_3:Er/Si devices decrease rapidly from 10 K to 70 K and 40 K (Fig. 3(b)), respectively. After that temperature for both devices, η is almost linear with the increase of temperature. The $^{\eta kT}/_{q}$ vs. $^{kT}/_{q}$ curve is plotted (Fig. 3(b)(inset)) to find out the actual current conduction mechanism and the origin of high η values for the diodes at low temperature [31]. For the Au/In_2O_3/Si and Au/In_2O_3:Er/Si devices, the intercepts of the linear fits of $^{\eta kT}/_{q}$ vs. $^{kT}/_{q}$ curves to the $^{\eta kT}/_{q}$ axis are at ~637 meV and at ~521 meV, respectively. These intercepts are known as the tunneling parameters of the Schottky diode [31,32]. The tunneling parameter values are $\gg thermal\ voltage\ \left(^{kT}/_{q}\right)$, which basically initiates the free carrier generation due to field emission (FE) in the devices [33]. On the other hand, very low barrier height at 10 K of 16 meV and 22 meV are calculated for both Au/In_2O_3/Si and Au/In_2O_3:Er/Si devices, respectively (Fig. 3(b)). A linear increase in barrier height (Φ_B) is observed with increasing temperature up to 0.63 eV and 0.66 eV, respectively for Au/In_2O_3/Si and Au/In_2O_3:Er/Si devices at 300 K (Fig. 3(b)). Therefore, at low temperatures, the electrons overcome the low barrier height by collecting the energy from the applied electric field and tunnel through the barrier. But, at high temperatures, the carriers collect energy from thermal agitation and applied electric field to overcome the large barrier height, which is known as thermionic field emission (TFE) process. The increase in η and a decrease in Φ_B of the diode at low temperatures might be due to the structural defects in the semiconductor, inhomogeneous doping, interface roughness and inhomogeneity of the thickness of the layer which were previously explained experimentally and theoretically [32–35]. In our case, the TFs were fabricated using spin coating technique, which involves considerable surface roughness and non-uniformity in the thickness of the TFs on the substrate. Similar type of temperature-dependent electrical properties of Pt Schottky contacts

to *n*-type GaN was successfully explained by Phark et al with the help of TE and TFE models [36].

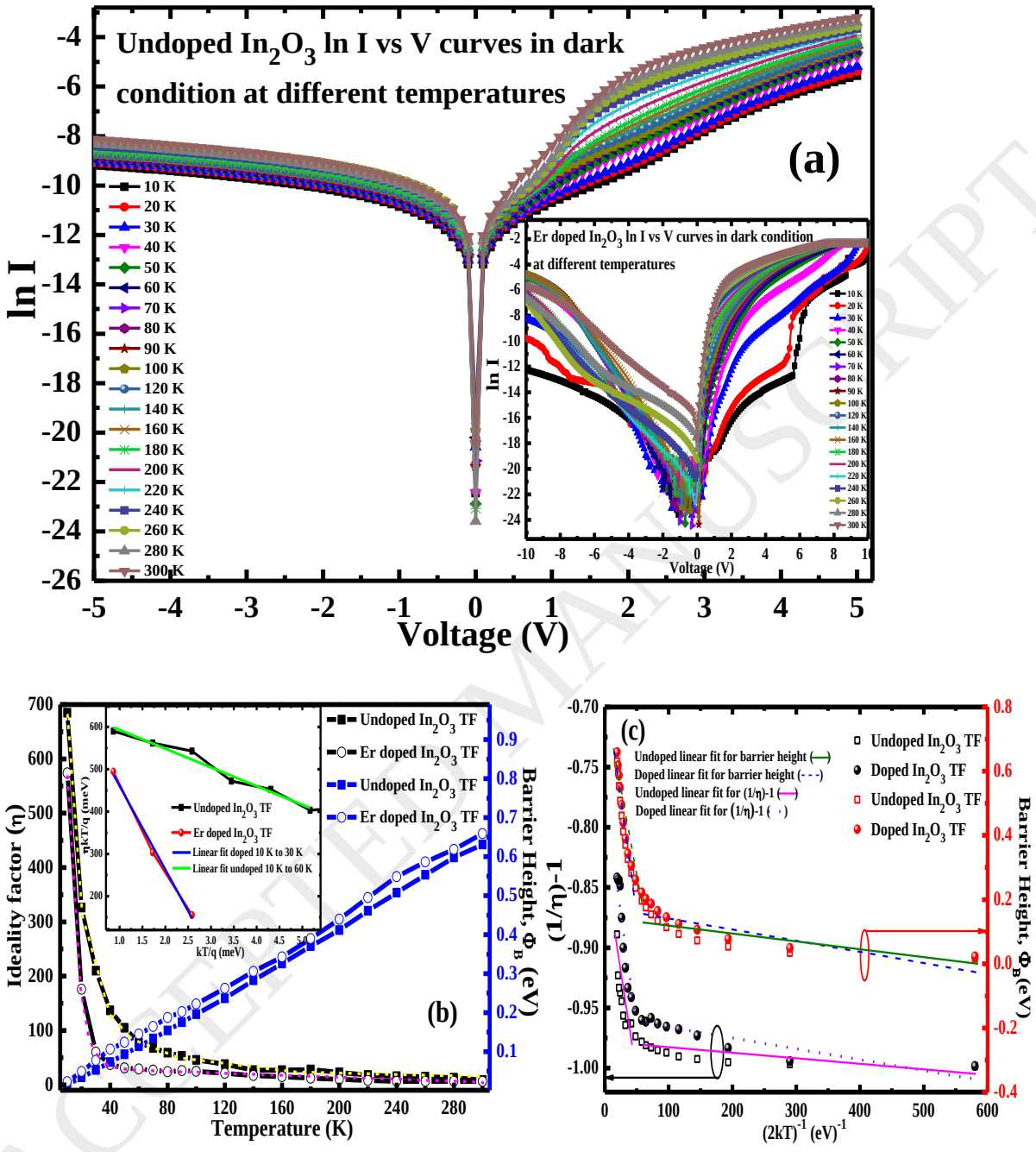

Fig. 3: (a) Temperature dependent dark ln I -V characteristics of the Au/In_2O_3/Si and Au/In_2O_3:Er/Si devices (inset); (b) temperature vs. ideality factor and barrier height curves fitted with non-linear curves, $^{\eta kT}/_{q}$ vs. $^{kT}/_{q}$ curves (inset); (c) $\left(\frac{1}{\eta}-1\right)$ vs. $(2kT)^{-1}$ and $(2kT)^{-1}$ vs. barrier height (Φ_B) plots fitted with straight lines.

According to Schmitsdorf et al [37], the linear variation of Schottky barrier height with temperature is due to the presence of barrier irregularity, which may create double Gaussian

distributions of the barrier heights at the junction [32,38]. Fig. 3(c) shows the $\left(\frac{1}{\eta} - 1\right)$ vs. $(2kT)^{-1}$ and $(2kT)^{-1}$ vs. Φ_B plots, which are fitted by two different lines of different slopes instead of a single straight line for the Au/In_2O_3/Si and Au/In_2O_3:Er/Si devices. The rapid changes in slope of the linear fits are occurring at 70 K for both devices. These two different slopes at the lower and higher temperature range represents the distinct activated process due to the existence of two Gaussian distributions [38] of barrier heights at the interface between TF and Schottky metal (Au) contact. At high temperatures the carriers overcome the higher barrier height and at low temperatures the carriers can only overcome the lower barrier height.

3.4. Temperature dependent photosensitivity and function of defects:

The dark current for the devices is plotted in Fig. 4(a) at an applied voltage of -2 V and at different temperatures from 10 K to 300 K. At 300 K the current produced by the Au/In_2O_3/Si device (-5.34 x 10^{-6} A) was higher than Au/In_2O_3:Er/Si device (-3.83 x10^{-6} A). The higher free carrier concentration (~8 x 10^{16} cm^{-3}) of undoped In_2O_3 TF as compared to In_2O_3:Er TF (~5 x 10^{12} cm^{-3}) produces large current in the undoped device [4]. With the decrease in temperature from 300 K to 10 K, the resistance of the undoped In_2O_3 TF decreased linearly due to the continuous trapping of the free carriers into the defect states. On the other hand, small amount of defects present in the In_2O_3:Er TF suddenly trapped the minority free carriers existing in the system at around ~280 K. Below this temperature, down to 10 K the Au/In_2O_3:Er/Si TF device possesses almost constant current because of the non-availability of free carriers in the film. Hence, the In_2O_3:Er TF possesses low current conductivity all over the temperature range. The photosensitivity (light current/dark current) of the devices were examined under UV light excitation (wavelength =340 nm) at different temperatures ranging from 10 K to 300 K (Fig. 4(b)). In the case of Au/In_2O_3/Si device, the sensitivity decreased gradually from 300 K to 140 K, which may be due to the Auger scattering of the

photogenerated carriers and residual carriers inside the TF. After 140 K the maximum electrons (due to low kinetic energy) are trapped into the defects and only the photoexcited carriers reach the electrodes effectively. In addition, those electrons trapped near the conduction band edge defects states are easier to promote to the conduction band by photon excitation for conduction process. Therefore, the photosensitivity of the device again increases from 140 K to 10 K. The increased photosensitivity of the Au/In_2O_3/Si device is a further evidence of defect states that are present in the material. For the Au/In_2O_3:Er/Si device the photosensitivity is almost linear up to

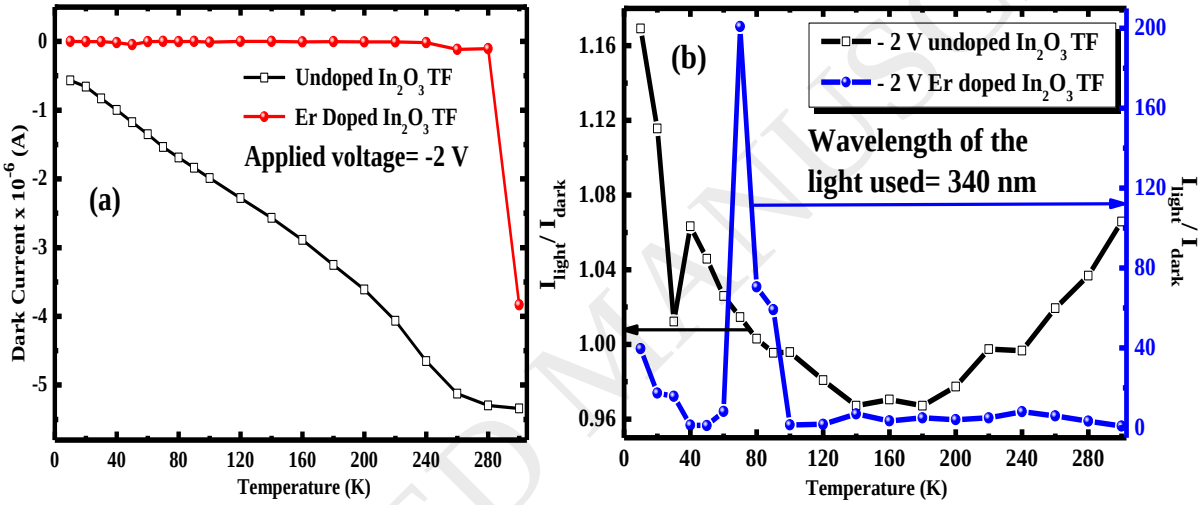

Fig. 4: (a) The dark current of the devices at an applied bias of -2 V against different applied temperature from 10 K to 300 K; (b) photosensitivity (light current/dark current) of the devices under UV light excitation (wavelength =340 nm) at different temperature ranging from 10 K to 300 K.

100 K, which may be due to the non-availability of the excess free carriers in the conduction band even after photon excitation. Beyond this temperature, a sudden rise in photosensitivity has been observed at ~70 K, which may be due to the Peierls phase transition [39]. A Peierls transition is basically defined as a metal insulator transition, when it reaches the Peierls temperature (T_p). Above T_p, the atoms are all equally spaced with the lattice constant 'a'. Below T_p, a distortion happens and the periodicity doubles to '2a', because of electron-phonon interactions in the conduction band. This process is called dimerization and happens

spontaneously when the material is cooled down. As a result the atoms form chains in one direction, which enhance the electric conductivity of the material suddenly. In this case the Peierls temperature (T_p) was found at ~70 K. The compensated carriers then become free at 70 K due to high internal thermal fluctuation in the In_2O_3:Er lattice, which was not observed for the highly defective undoped In_2O_3 TF. Similar effects have also been observed for the In_2O_3-SiOx heterostructure based 1D system at 160 K [40]. The sensitivity of the Au/In_2O_3:Er/Si device falls suddenly at 60 K and again a small rise is detected up to 10 K. It is important to point out that over the whole temperature range the photosensitivity of Au/In_2O_3:Er/Si device shows greater value as compared to Au/In_2O_3/Si device (at -2 V bias) with maximum of ~200 times at 70 K. Furthermore, the Au/In_2O_3/Si device shows small variation in photosensitivity (~1.09 times), whereas the In_2O_3:Er TF produced significant deviation in photosensitivity (~50 times) between the highest (300 K) and the lowest (10 K) points of temperature. This fact again demonstrates that the photoconduction process in undoped In_2O_3 TF and In_2O_3:Er TF is quite different. Trap states, which emit electrons under photon excitation, play a major role in the undoped In_2O_3 TF material for the whole temperature range. However, a little variation in photosensitivity has been observed between 300 K and 10 K due to the presence of large residual current (dark current). Again, the In_2O_3:Er TF is almost free from defects, so trap related photoconduction is not observed up to 60 K. Whereas at a very low temperature from 50 K to 10 K the small concentration of defects near the conduction band edge starts to de-trap the electrons (similar to Au/In_2O_3/Si device) under photon excitation. But this process has produced massive variation in photosensitivity of the doped device due to the presence of small residual current. Finally, it can be concluded that the In_2O_3:Er TF is not completely free from defects, and shallow traps in In_2O_3 play a major role in photoconduction for In_2O_3:Er TF at very low temperature.

3.5 Low-temperature responsivity and defect states:

The wavelength dependent (300 nm -500 nm) responsivity of the devices was measured at 10 K to find out the energy positions of trap states in the material. Fig. 5(a) displays the responsivity curves for both devices under the applied reverse bias of -5 V, respectively. The Au/In_2O_3/Si device shows a sharp rise in photoresponsivity (50.36 A/W) from near band edge transition at 380 nm (~ 3.26 eV), due to the presence of trap states as previously reported by the authors [4]. At 10 K, there is no significant detection related to the main band gap (at 350 nm) of In_2O_3. The transition at 410 nm was also detected for defect level in the undoped material [41]. But in the case of Au/In_2O_3:Er/Si device, a broadband from 330 nm - 370 nm (~3.75 eV- 3.35 eV) was obtained. The authors reported previously that the band gap of highly Er doped In_2O_3 TF shifted to 324 nm (~3.82 eV) [4]. Therefore, the photoconductivity of the In_2O_3:Er TF based device at 330 nm (~3.75 eV) is related to the main band transition. Above that wavelength the shallow level defect transitions produced photoconductivity up to 370 nm (~3.35 eV). All possible transitions for both devices are represented schematically in Figs. 5(b) and 5(c). These explain the key role of minor defects that are present into the In_2O_3:Er TF during low-temperature photoconduction. The In_2O_3:Er has a dominant defect at 410 nm (~3.02 eV), and its responsivity spectrum is shown in Fig. 5(a). But the ratio of maximum responsivity in the UV region to the responsivity in the visible region at 410 nm is higher (~3) for Au/In_2O_3:Er/Si device as compared with Au/In_2O_3/Si device (~1.1). Therefore, it may be concluded that Er had definitely reduced the density of defects into the In_2O_3 up to a certain level, which improved the UV-Visible rejection ratio of the In_2O_3:Er TF based detector.

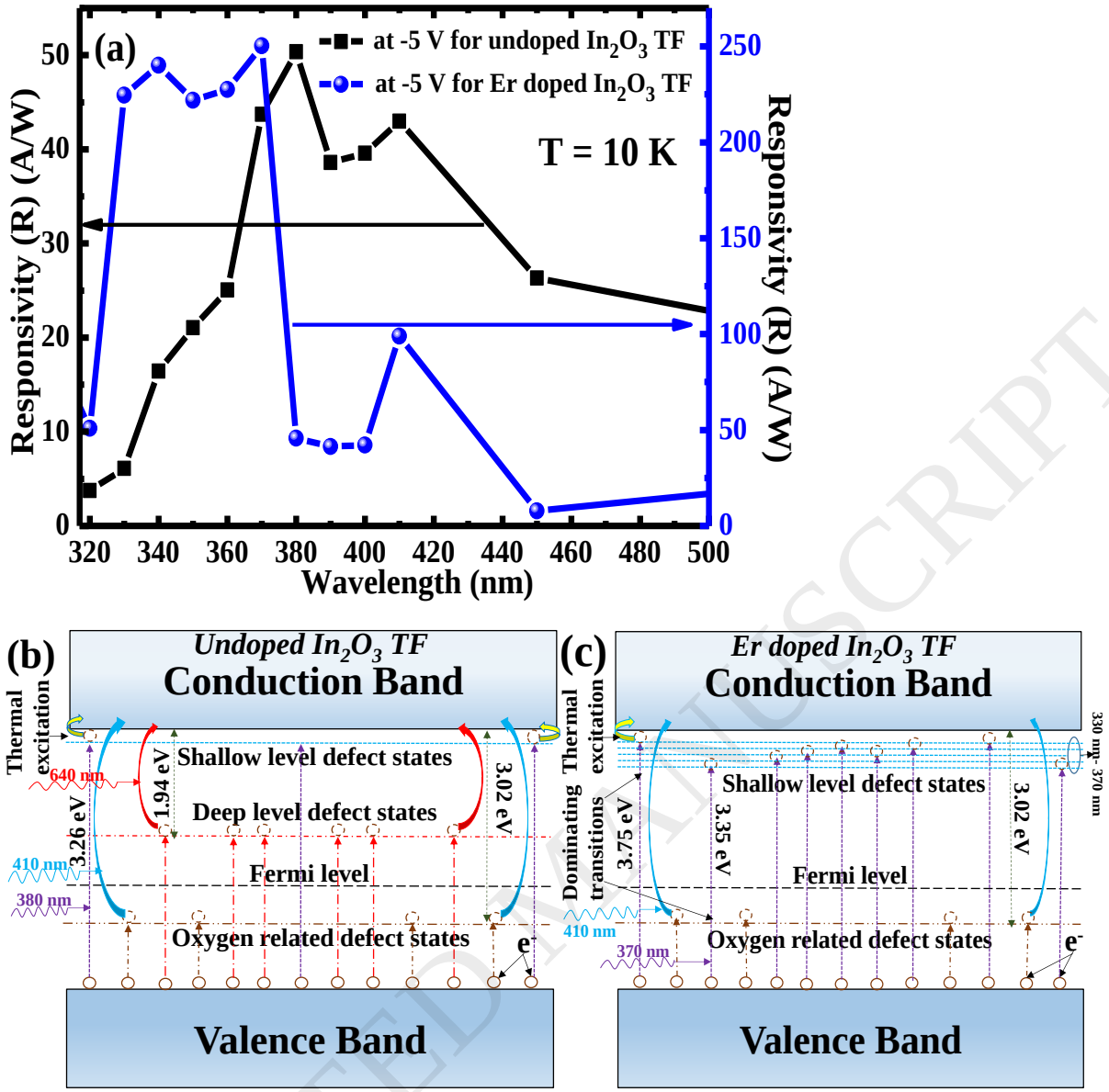

Fig. 5: (a) Responsivity (A/W) vs wavelength (nm) curves for Au/In_2O_3/Si and Au/In_2O_3:Er/Si devices under the applied bias of -5 V; schematic band diagram with the different transitions for (b) undoped In_2O_3 TF and (c) In_2O_3:Er TF.

Fig. 6 shows the temporal response of the undoped In_2O_3 (Fig. 6(a)) and In_2O_3:Er TF based detector (Fig. 6(b)) at 10 K under white light, red light (640 nm) and UV light (340 nm) illumination at an applied bias voltage of -5 V. The incident light dependent current-time (I-t) characteristics of the detectors have been measured with the light on/off switching irradiation with a time interval of 5 s. Under white light illumination, the calculated rise (T_r) and fall (T_f) times for Au/In_2O_3/Si and Au/In_2O_3:Er/Si devices are ~135 ms and ~130 ms, and ~132 ms and ~125 ms, respectively. The Au/In_2O_3:Er/Si device has a faster response as compared to

Au/In_2O_3/Si device, which may be due to the removal of defects. Both devices were illuminated by 640 nm wavelength of light (as it is reported that the oxygen-related defect state can produce optical transition process at the same energy level) [42] to verify the oxygen defect related photoconductivity.

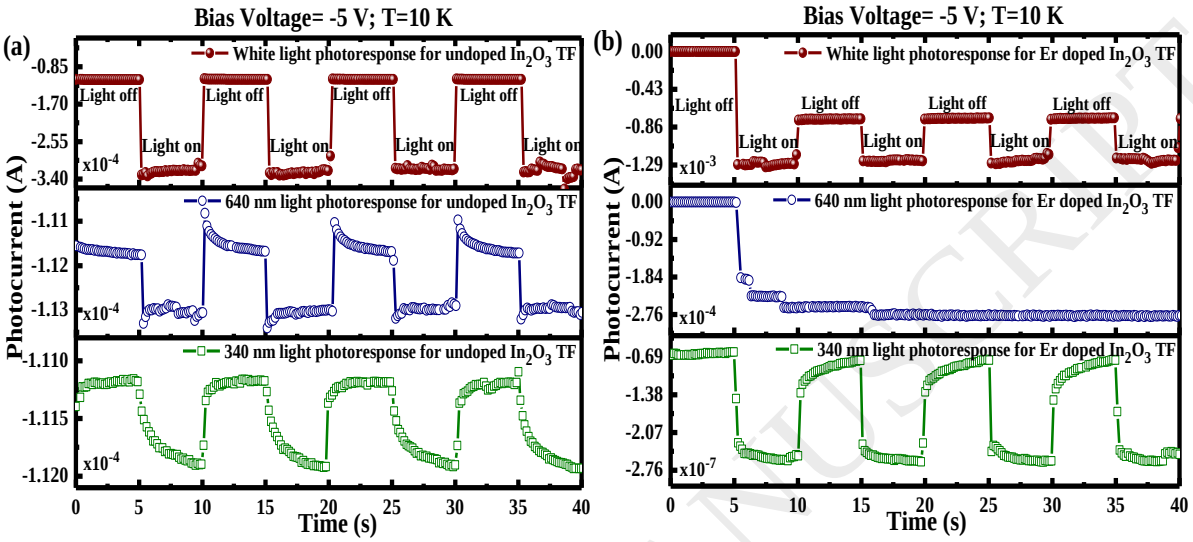

Fig. 6: Time-dependent photocurrent for the detectors at 10 K under white light, red light (640 nm) and UV light (340 nm) illumination at the biasing voltage of -5 V for (a) Au/In_2O_3/Si and (b) Au/In_2O_3:Er/Si devices.

The undoped In_2O_3 TF device shows the usual behaviour under 640 nm light on/off switching irradiation, with T_r ~ 108 ms and T_f ~ 106 ms. The Au/In_2O_3:Er/Si device did not respond to the illumination of 640 nm, which may be due to the removal of corresponding oxygen-related defects. The corresponding transitions are shown in Figs. 5(b) and 5(c). The light on/off switching irradiation experiment was performed for Au/In_2O_3/Si and Au/In_2O_3:Er/Si devices under 340 nm near the band gap energy. The doped device (T_r ~400 ms, T_f ~245 ms) shows superior performance as compared to the undoped In_2O_3 TF device (T_r ~501 ms, T_f ~2 s). We can conclude from the above observations that the Au/In_2O_3:Er/Si device acts as good UV detector, which selectively detects UV light with higher response speed and also the oxygen-related defect states at 640 nm has been removed. However, some of the defects still remain (410 nm, as pointed out from responsivity spectrum) in the material after Er doping of the In_2O_3 lattice.

4. Conclusion:

In conclusion, we have successfully synthesised undoped and In_2O_3:Er TFs by a simple, cost-effective sol-gel, spin-on technique. The doping of Er in the In_2O_3 lattice was confirmed by the formation of an inhomogeneous In-O-Er layer using SIMS analysis. The reduction ratio in current window for In_2O_3:Er TF was lesser than undoped In_2O_3 TF due to the reduction of oxygen defects present in the In_2O_3 parent host. The calculated low saturation current (~2.1 x 10^{-6} A) and ideality factor (η~6) of Au/In_2O_3:Er/Si device as compared to Au/In_2O_3/Si device (~9.8 x 10^{-6} A and η~12), could indicate the removal of defect states by Er from In_2O_3 lattice. The forward I–V characteristics are analysed on the basis of standard TE and TFE theory and on the assumption of a double Gaussian distribution of the barrier heights. According to TFE theory it has been shown that η decreases while Φ_B increases with increasing temperatures. The presence of large density of defects play a major role in the photoconduction process in the whole temperature range for Au/In_2O_3/Si device, whereas a much smaller number of shallow level defects assist in the photoconduction at very low temperatures from 50 K -10 K for Au/In_2O_3:Er/Si device. The In_2O_3:Er TF shows a ~50 nm (~0.5 eV) blue shift in main bandgap transition as compared to undoped In_2O_3 TF at 10 K. The In_2O_3:Er based detector shows higher UV to visible cut off ratio (~3 times) and improved temporal response in the UV region due to removal of defects. Finally, Au/In_2O_3:Er/Si device performed better and reliably as UV detector despite that some defects still remain in the In_2O_3 lattice.

Acknowledgements:

The authors gratefully acknowledge SAIF, I.I.T. Bombay for providing ToF-SIMS facility. The authors would also like to acknowledge N.I.T. Durgapur, CSIR (03(1355)/16/EMR-II) and Govt. of India for financial support.

References:

[1] K. Ellmer, Past achievements and future challenges in the development of optically transparent electrodes, Nat. Photonics. 6 (2012) 808–816. doi:10.1038/nphoton.2012.282.

[2] H. S. Kim, P. D. Byrne, A. Facchetti, T. J. Marks, High Performance Solution-Processed Indium Oxide Thin-Film Transistors, J. Am. Chem. Soc. 130 (2008) 12580–12581. doi: 10.1021/ja804262z.

[3] D. Liu, W. W. Lei, B. Zou, S. D. Yu, J. Hao, K. Wang, B. B. Liu, Q. L. Cui, G. T. Zou, High-pressure x-ray diffraction and Raman spectra study of indium oxide, J. Appl. Phys. 104 (2008) 083506. doi:10.1063/1.2999369.

[4] A. Ghosh, A. Mondal, A. Das, S. Chattopadhyay, K. K. Chattopadhyay, Removal of oxygen related defects from chemically synthesized In_2O_3 thin film doped with Er by spin-on technique, J. Alloys Compd. 695 (2017) 1260–1265. doi:10.1016/j.jallcom.2016.10.254.

[5] J. H. Noh, S. Y. Ryu, S. J. Jo, C. S. Kim, S. Sohn, P. D. Rack, D. Kim, H. K. Baik, Indium Oxide Thin-Film Transistors Fabricated by RF Sputtering at Room Temperature, IEEE Elec. Dev. Lett. 31(6) (2010) 567–569. doi: 10.1109/LED.2010.2046133.

[6] H. Yabuta, M. Sano, K. Abe, T. Aiba, T. Den, H. Kumomi, K. Nomura, T. Kamiya, H. Hosno, High-mobility thin-film transistor with amorphous InGaZnO4 channel fabricated by room temperature rf-magnetron sputtering, Appl. Phys. Lett. 89 (2006) 112123. doi:10.1063/1.2353811.

[7] K. Nomura, H. Ohta, K. Ueda, T. Kamiya, M. Hirano, H. Hosono, Thin-Film Transistor Fabricated in Single-Crystalline Transparent Oxide Semiconductor, Science 300 (2003) 1269-1272. doi:10.1126/science.1083212.

[8] L. Qin, Y. Huang, T. Tsuboi, H. J. Seo, The red-emitting phosphors of Eu 3 + -activated MR 2 (MoO 4) 4 (M = Ba , Sr , Ca ; R = La3+, Gd3+, Y3+) for light emitting diodes, Materials Research Bulletin 47 (2012) 4498–4502. doi:10.1016/j.materresbull.2012.10.004.

[9] T. Minami, T. Yamamoto, T. Miyata, Highly transparent and conductive rare earth-doped ZnO thin films prepared by magnetron sputtering, Thin Solid Films 366 (2000) 63–68. doi:10.1016/S0040-6090(00)00731-8.

[10] Q. Xiao, H. Zhu, D. Tu, E. Ma, X. Chen, Near-Infrared-to-Near-Infrared Downshifting and Near-Infrared-to- Visible Upconverting Luminescence of Er 3 + -Doped In 2 O 3 Nanocrystals, J. Phys. Chem. C 117(20) (2013) 10834. doi:10.1021/jp4030552.

[11] D. Maestre, E. Hernandez, A. Cremades, M. Amati, J. Piqueras, Synthesis and Characterization of Small Dimensional Structures of Er-Doped SnO 2 and Erbium − Tin − Oxide, Cryst. Growth Des. 12 (2012) 2478. doi:10.1021/cg300106k.

[12] M. Fasoli, A. Vedda, M. Nikl, C. Jiang, B. P. Uberuaga, D. A. Andersson, K. J. Mcclellan, C. R. Stanek, Band-gap engineering for removing shallow traps in rare-earth Lu 3 Al 5 O 12 garnet scintillators using Ga 3 + doping, Phys. Rev. B 84 (2011) 81102. doi:10.1103/PhysRevB.84.081102.

[13] H. Liu, M. Luo, J. Hu, T. Zhou, R. Chen, J. Li, β-Bi2O3 and Er3+ doped β-Bi2O3 single crystalline nanosheets with exposed reactive { 0 0 1 } facets and enhanced photocatalytic performance, Applied Catal. B, Environ. 140–141 (2013) 141–150. doi:10.1016/j.apcatb.2013.04.009.

[14] K. Lorenz, E. Nogales, S. M. C. Miranda, N. Franco, B. Mendez, E. Alves, G. Tourbot, B. Daudin, Enhanced red emission from praseodymium-doped GaN nanowires by defect engineering, Acta Materialia 61 (2013) 3278–3284.

doi:10.1016/j.actamat.2013.02.016.

[15] S. Dhar, N. Halder, A. Mondal, B. Bansal, B. M. Arora, Detailed studies on the origin of nitrogen-related electron traps in dilute GaAsN layers grown by liquid phase epitaxy, Semicond. Sci. Technol. 20 (2005) 1168. doi:10.1088/0268-1242/20/12/004.

[16] H. K. Kim, C. C. Li, G. Nykolak, P. C. Becker, Photoluminescence and electrical properties of erbiumdoped indium oxide films prepared by rf sputtering, J. Appl. Phys. 76, (1994) 8209-8211. doi:10.1063/1.357882.

[17] S. Abedrabbo, B. Lahlouh, A.T. Fiory, Analytical study of thermal annealing behaviour of erbium emission in Er 2 O 3 -sol – gel silica films, J. Phys. D: Appl. Phys. 44 (2011) 315401. doi:10.1088/0022-3727/44/31/315401.

[18] T. Lin, X. Zhang, J. Xu, X. Liu, M.T. Swihart, L. Xu, K. Chen, Strong energy-transfer-induced enhancement of Er3+ luminescence in In2O3 nanocrystal codoped silica films, Appl. Phys. Lett. 103 (2013) 181906. doi:10.1063/1.4827883.

[19] S. Manna, R. Aluguri, R. Bar, S. Das, N. Prtljaga, L. Pavesi, S.K. Ray, Enhancement of photoluminescence intensity of erbium doped silica containing Ge nanocrystals : distance dependent interactions, Nanotechnology. 26 (2015) 45202. doi:10.1088/0957-4484/26/4/045202.

[20] D. Liang, J.E. Bowers, Recent progress in lasers on silicon, Nat. Photonics 4 (2010) 511–517. doi:10.1038/NPHOTON.2010.167.

[21] I. Nakamura, N. Negishi, S. Kutsuna, T. Ihara, S. Sugihara, K. Takeuchi, Role of oxygen vacancy in the plasma-treated TiO 2 photocatalyst with visible light activity for NO removal, J. Mol. Catal. A Chem. 161 (2000) 205–212. doi: 10.1016/S1381-1169(00)00362-9.

[22] X. Pan, M. Yang, X. Fu, N. Zhang, Y. Xu, Defective TiO 2 with oxygen vacancies: synthesis, properties and photocatalytic applications, Nanoscale 5 (2013) 3601–3614. doi:10.1039/c3nr00476g.

[23] N. A. A. Saqri, A. Mondal, J. F. Felix, Y. G. Gobato, V. O. Gordo, H. Albalawi, D. Jameel, H. Alghamdi, F. A. Mashary, D. Taylor, M. S. A. El-sadek, M. Henini, Investigation of defects in indium doped TiO 2 thin fi lms using electrical and optical techniques, J. Alloys Compd. 698 (2017) 883–891. doi:10.1016/j.jallcom.2016.12.294.

[24] A. Walsh, Surface oxygen vacancy origin of electron accumulation in indium oxide, Appl. Phys. Lett. 98 (2011) 261910. doi:10.1063/1.3604811.

[25] J. J. Meléndez, M. Weirzbowska, In 2 O 3 Doped with Hydrogen: Electronic Structure and Optical Properties from the Pseudopotential Self-Interaction Corrected Density Functional Theory and the Random Phase Approximation, J. Phys. Chem. C 120(7) (2016) 4007. doi:10.1021/acs.jpcc.5b11753.

[26] K. Iltgen, C. Bendel, A. Benninghoven, E. Niehuis, Optimized time-of-flight secondary ion mass spectroscopy depth profiling with a dual beam technique Optimized time-of-flight secondary ion mass spectroscopy depth profiling with a dual beam technique, J. Vac. Sci. Technol. A 15 (1997) 460. doi:10.1116/1.580874.

[27] A.J. Atanacio, J. Nowotny, K.E. Prince, Reactivity between In 2 O 3 and TiO 2 (rutile) studied using secondary ion mass spectrometry (SIMS), Sep. Purif. Technol. 91 (2012) 96–102. doi:10.1016/j.seppur.2011.11.013.

[28] Y. Zhang, J. Li, D. Fang, Oxygen-vacancy-induced memory effect and large recoverable strain in a barium titanate single crystal, Phy. Rev. B 82 (2010) 064103. doi:10.1103/PhysRevB.82.064103.

[29] X. Wang, C. Hu, Y. Song, X. Zhao, L. Zhang, Z. Lv, Y. Wang, Z. Liu, Y. Wang, Y. Zhang, Y. Sui, B. Song, Effect of Oxygen-deficiencies on Resistance Switching in Amorphous YFe0.5Cr0.5O3−d films, Sci. Rep. 6 (2016) 30335. doi:10.1038/srep30335.

[30] I. Hussain, M. Y. Soomro, N. Bano, O. Nur, M. Willander, Systematic study of interface trap and barrier inhomogeneities using I-V-T characteristics of Au / ZnO nanorods Schottky diode, J. Appl. Phys. 113 (2013) 234509. doi:10.1063/1.4810924.

[31] M.K. Hudait, S.B. Krupanidhi, Doping dependence of the barrier height and ideality factor of Au / n-GaAs Schottky diodes at low temperatures, Physica B 307 (2001) 125–137. doi:10.1016/S0921-4526(01)00631-7.

[32] J.H. Werner, H.H. Güttler, Barrier inhomogeneities at Schottky contacts, J. Appl. Phys. 69 (1991) 1522-1533. doi:10.1063/1.347243.

[33] H. Cetin, E. Ayyildiz, Temperature dependence of electrical parameters of the Au / n-InP Schottky barrier diodes, Semicond. Sci. Technol. 20 (2005) 625-631. doi:10.1088/0268-1242/20/6/025.

[34] Y. P. Song, R. L. V. Meirhaeghe, W. H. Laflere, F. Cardon, On the difference in apparent barrier height as obtained from capacitance-voltage and current-voltage-temperature measurements on Al/*p*-InP Schottky barriers, Solid-State Electronics 29(6) (1986) 633–638. doi:10.1016/0038-1101(86)90145-0.

[35] J. P. Sullivan, R. T. Tung, M. R. Pinto, W. R. Graham, Electron transport of inhomogeneous Schottky barriers : A numerical study, J. Appl. Phys. 70 (2012) 7403-7424. doi:10.1063/1.349737.

[36] S. Phark, H. Kim, K. M. Song, P. G. Kang, H. S. Shin, D. Kim, Current transport in Pt

Schottky contacts to a -plane n-type GaN, J. Phys. D: Appl. Phys. 43, (2010) 165102. doi:10.1088/0022-3727/43/16/165102.

[37] R. F. Schmitsdorf, T. U. Kampen, W. Monch, Correlation between barrier height and interface structure of Ag / Si (111) Schottky diodes, Surf. Science 324, (1995) 249-256. doi:10.1016/0039-6028(94)00791-8

[38] N. N. K. Reddy, V. R. Reddy, Barrier characteristics of Pt / Ru Schottky contacts on n -type GaN based on I – V – T and C – V – T measurements, Bull. Mater. Sci. 35(1) (2012) 53–61. doi:10.1007/s12034-011-0262-6

[39] J. Yang, F. Lu, Y. Li, S. Yang, R. Li, N. Huo, C. Fan, Z. Wei, J. Li, S. Li, Low temperature electrical transport and photoresponsive properties of H-doped MoO nanosheets, J. Mater. Chem. C 2 (2014) 1034. doi:10.1039/C3TC32142H.

[40] A. Mondal, N. K. Singh, P. Chinnamuthu, J. C. Dhar, A. Bhattacharyya, S. Choudhury, Enlarged photodetection using SiOx nanowire arrays, IEEE Photonics Technol. Lett. 24 (2012) 2020–2023. doi:10.1109/LPT.2012.2218232.

[41] J. Gan, X. Lu, T. Zhai, Y. Zhao, S. Xie, Y. Mao, Y. Zhang, Y. Yang, Y. Tong, Vertically aligned In 2 O 3 nanorods on FTO substrates for photoelectrochemical applications, J. Mater. Chem. 21 (2011) 14685–14692. doi:10.1039/c1jm11774b.

[42] W.J. Kim, D. Pradhan, Y. Sohn, Fundamental nature and CO oxidation activities of indium oxide nanostructures: 1D-wires, 2D-plates, and 3D-cubes and donuts, Journal of Materials Chemistry A 1 (2013) 10193–10202. doi:10.1039/c3ta12312j.